https://doi.org/10.1016/j.ces.2021.117058

Household slow sand filters operating in continuous and intermittent flows: computational fluid dynamics simulation and validation by tracer experiments

Liri Yoko Cruz Prieto Hojo[a]; Ricardo Vicente de Paula Rezende[c]; Sandro Rogério Lautenschlager[b]; Lyda Patricia Sabogal-Paz[a]

[a] Department of Hydraulics and Sanitation, São Carlos School of Engineering, University of São Paulo, Trabalhador São-Carlense Avenue, 400, São Paulo 13566-590, Brazil.

[b] Maringá State University, Technology Center, Department of Civil Engineering, Colombo Avenue, 5790, Maringá 87020900, Paraná, Brazil.

[c] Maringá State University, Technology Center, Department of Chemical Engineering, Colombo Avenue, 5790, Maringá 87020900, Paraná, Brazil.

[a] Email: lysaboga@sc.usp.br

Abstract

This paper analysed geometries and flows in household slow sand filters (HSSFs) through computational fluid dynamics (CFD) to evaluate the hydrodynamics of filters. Four HSSFs in full scale were studied with a capacity to produce 48 $L.d^{-1}$ each with diameters of 190 mm and 250 mm and with a filter medium depth of 0.5 meters. The

hydrodynamics of the four mathematical models of the HSSFs was validated using the experimental residence time distribution (RTD). The Kruskal Wallis non-parametric test indicates that the results of the experimental RTDs and the simulated RTDs did not show significant differences, therefore the mathematical models represent the physical models, which requires a detailed 3D analysis of the flow in the filters. The results showed that the HSSFs have a flow close to plug flow reactor. Internal recirculation zones were not found, nor short-circuit ones; however, dead zones were verified at the base of the filter with volumes below 3% when compared to the total volume of the filtering and draining layers, not necessary to make changes in geometry. The results of the computational simulation showed that the continuous filters had a smaller velocity variation and the filters with smaller diameter presented a reduction in dead zones when compared to the filters with larger diameters operated in the same flow regime. The study focused on the hydraulic aspects of HSSFs, but it is noteworthy that the choice of the type of operation to be adopted by families that use this type of treatment depends on studies that assess the efficiency of water treatment filters that were not considered in this work.

Keywords: biosand filter, computational fluid dynamics (CFD); drinking water; residence time distribution (RTD); software *ANSYS Fluent*

1. Introduction

The ingestion of water contaminated by feces, the lack of collection and treatment of sanitary sewage and inadequate hygiene habits are the causes of about 4 billion diarrheal diseases per year, and out of these 1.8 million are fatal (UNEP, 2016). According to Dadonaite et al. (2020), in 2016, it was estimated that 1.55 million deaths

were caused by diarrheal diseases worldwide and, in 2017, that number increased to 1.6 million; one third of whom were children under the age of five.

An inexpensive and efficient way to empower people without access to water, both in urban and rural areas that are not provided with a distribution network, is to use the so-called point-of-use treatment technologies (POU) and, among them, Household Slow Sand Filters (HSSFs) can be highlighted (Sobsey et al., 2008).

1.1. Features and functioning of HSSFs

HSSFs were adapted from conventional slow sand filters (SSFs) designed to operate in batch. Both the HSSF and the SSF allow the development of a biological layer on top of the granular medium that helps the treatment (CAWST, 2012; Maciel and Sabogal-Paz, 2020; Andreoli and Sabogal-Paz, 2020).

Research carried out on HSSFs showed how easy it is for a user to construct and operate them. These studies focus on evaluating the efficiency (Kennedy et al., 2012; Maciel and Sabogal-Paz, 2020; Terin and Sabogal-Paz, 2019; Sabogal-Paz et al 2020; Andreoli and Sabogal-Paz, 2020).

The fundamentals of HSSF contaminant removal are the combination of physical and biological processes. According to Jadhav, Husain and Chavan (2015), physical mechanisms include retention of particles in the pores of the filter media and an adsorption, which allows for organic removal, while biological components include predation, elimination, natural death/inactivation and partial reduction of organic carbon due to the metabolism of the microorganism. Therefore, the HSSF treats water by a combination of physical processes with biological activity present on the surface of the filter layer (*schmutzdecke*).

The I-HSSF can operate with a filtration rate of up to 26.4 $m^3.m^{-2}.day^{-1}$ (Elliot et al., 2006) and the recommended pause period is in the range of 1 to 48 hours (Cawst, 2012).

The continuous flow filter (C-HSSF) can be operated with a lower filtration rate, up to 9.6 $m^3.m^{-2}.day^{-1}$ (Maciel and Sabogal-Paz, 2020) and its feeding can be by gravity or direct pumping, if there is a control of the filtration rate (Sabogal-Paz et al., 2020).

In the intermittent flow filter (I-HSSF), the water to be treated must be maintained in the filter medium pores between each batch feed, generating the pause period that is important as it allows physical and biological processes to occur to treat water (Sabogal-Paz et al 2020). The study developed by Elliott et al. (2008) showed that the best filter performance occurs when the volume of water to be treated is close to the pore volume.

In the study by Maciel and Sabogal-Paz (2020), continuous filters operated at a filtration rate of 0.68 $m^3.m^2.day^{-1}$ obtained residence time distribution (RTDs) of 991 min. and 876 min. with a turbidity reduction of 89.4% and 83.8%, respectively, and the intermittent filters showed turbidity removal of 91.8 and 90.5%. Terin and Sabogal-Paz (2019) worked with HSSF operating in continuous flow at a filtration rate of 1.22 $m^3.m^2.day^{-1}$. and obtained a turbidity reduction of 84.39% for the RTD 417 min. and the filter intermittent showed a reduction in turbidity of 81.41% for the 4-hour pause period and 83.78% for the 12-hour pause period.

The C-HSSF was classified as a piston flow reactor by Maciel and Sabogal-Paz (2018), Sabogal-Paz et al. (2020), Terin and Sabogal-Paz (2019) and Young-Rojanschi and Madramootoo (2014b), there is a gap in these studies in terms of not analyzing the influence of possible short circuits and dead zones on residence time and quality of

water. This question was addressed in the present study using the CFD to analyze the DTR, the type of flow and possible short-circuit influences and dead zones.

1.2. Tracer test

The simplest and most direct way to determine the residence time distribution (RTD) is to use a non-reactive tracer, using the stimulus and response technique. Various types of experiments can be used with pulse and/or step type stimuli (Levenspiel, 1999).

In real chemical reactors, in general, they tend to deviate from ideality, but for the hydrodynamic characterization of reactors the ideal flows are considered for modelling, which are: Plug Flow Reactor - (PFR) and Continuous Stirred Tank Reactor – (CSTR) (Levenspiel, 1999). In the studies by Andreoli and Sabogal-Paz (2020), Bradley et al. (2011), Elliott et al. (2008), Maciel and Sabogal-Paz (2020), Lynn et al. (2013), Sabogal-Paz et al. (2020) and Terin and Sabogal-Paz (2019), the hydraulic behaviour of the I-HSSF was evaluated and classified as a plug flow reactor. The C-HSSF was also classified as a plug flow reactor by Maciel and Sabogal-Paz (2020), Sabogal-Paz et al. (2020), Terin and Sabogal-Paz (2019), Young-Rojanschi and Madramootoo (2014a).

The necessary condition for plug flow reactors is that the residence time must be the same for all fluid elements (Levenspiel, 1999). Thus, the fluid passes through the filter without mixing the fluid from the front and back inlet, that is, without overflowing. It should be noted that in a plug flow reactor, the composition of the fluid varies from point to point along a flow path (Levenspiel, 1999). In this context, Elliott et al. (2008) evaluated an HSSF that showed a minimal effect of dispersion by flow paths through porous media. Therefore, the microbial removal process occurs

124 homogeneously in all water portions that enter the HSSF and advance with the depth in
125 the biological layer (Sabogal-Paz et al., 2020).
126
127 **1.3. Mathematical modelling and simulation of HSSFs**
128 Mathematical models can predict results from the control and operating
129 conditions defined by users to foresee improvements in a filtration process when
130 producing drinking water (Botari and Di Bernardo, 2012). The mathematical models
131 used in the CFD are obtained through differential or integral balances of the conserved
132 properties, that is, they adopt the principles of conservation of mass, momentum and
133 energy.
134 The CFD has become a robust tool in the reactor design and diagnosis process,
135 providing detailed information about the reactors, such as the velocity distribution field,
136 the concentration distribution and energy consumption (Zhang et al., 2007).
137 According to Langergraber et al. (2009), mathematical models were developed
138 and validated with experimental tests, thus they can be used to evaluate and improve
139 existing design criteria. The CFD is normally used in the tracer test simulation and
140 validated with the physical experiment tracer test (Brannock et al., 2010; Furman and
141 Stegowski, 2011; Gharibian et al., 2020; Klusener et al., 2007; Qi et al., 2013; Zhang et
142 al., 2007).
143
144 **1.4. Tracer test with CFD**
145 The comparison of the experimental RTD with the CFD by RTD prediction is
146 essential to ensure an acceptable precision of the mathematical model (Furman and
147 Stegowski, 2011).

148 Regarding the application of the RTD technique to filters, Qi et al. (2013)
149 performed tracer tests with CFD in an upstream sand filter with a length of 2.0 m and
150 width 1.0 m and flow rate of 25.2 $L.h^{-1}$ and determined the RTD to characterize the flow
151 in filters with two configurations, which are: the first, without a support layer, without a
152 layer of water on the filter layer and with a collector tube along the entire length in the
153 upper portion of the filter layer; and the second, with a support layer, with a layer of
154 water on the filter layer and with a collector tube in part of the upper portion of the filter
155 layer.

156 The CFD simulation, developed by Qi et al. (2013), indicated that the water
157 current lines had an upward and downward sloping direction, and the velocity in the
158 middle of the filter was the highest; about five times greater than the minimum. The
159 comparison of the experimental results with the CFD simulation concludes that the filter
160 that had the support layer, the water slide and partial collector tube eliminated the
161 preferred paths and the stagnation zones compared to the filter that did not have these
162 characteristics. In filters with preferential flow paths, it was proven that the RTD
163 obtained with CFD was lower than the calculated RTD.

164 Although there is research on the hydrodynamics of HSSFs, little has been
165 discussed about the influence of the outlet system on the hydrodynamics of filters
166 (Berbert et al., 2016). The study by Berbert et al. (2016) consisted of analysing the
167 influence of the HSSF output system on the hydrodynamics of the filters and three
168 different models operated in intermittent flow were simulated in the ANSYS-CFX
169 software: the PEU/ UEM model (Berbert et al., 2016), the CAWST version 10
170 (CAWST, 2012) and HydrAid (Kikkawa, 2008).

171 The filters of the CAWST and HydrAid models were simulated with the original
172 geometry that has an outlet system on the side and an outlet configuration with a

collector ring inside was simulated. In the PEU/UEM model, four types of localized outlets were simulated: in the center in an upward flow, on the side, at the bottom and a collector ring inside. The study concluded that the PEU/UEM filter that has a collector ring-shaped output with the interface downwards contributes to improving the current lines by creating a better distribution of velocity across the three axes, reducing dead zones and increasing hydraulic residence time (Berbert et al., 2016).

2. Materials and methods

2.1 Experimental

2.1.1 Construction and operation of HSSFs

Four HSSFs were evaluated, two in continuous flow (C-HSSFs) and two in intermittent flow (I-HSSFs). The filters were built with four layers of the same thickness composed of fine sand, coarse sand, fine gravel and coarse gravel, and above the fine sand there was a water slide, which is presented in detail in the supplementary material. The maximum water level above the filter layer was regulated by a float valve.

The C-HSSF1 was a continuous flow filter built in acrylic with a diameter of 190 mm and the C-HSSF2, which was also operated in continuous flow, however it was built in PVC with a diameter of 250 mm. The I-HSSF1 operated in an intermittent flow with a 190 mm diameter acrylic body and the I-HSSF2 had the same flow as the previous one, but it was built in PVC with a diameter of 250 mm. Filters with a diameter of 190 mm had a cross-sectional area of 0.028 m^2 and filters with a diameter of 250 mm had a cross-sectional area of 0.049 m^2. The base of the HSSFs consisted of a CAP-type connection, and in the center of that base an outlet tube (collector) was fitted with a tap to capture the filtered water.

The walls of C-HSSF1 and I-HSSF1 were covered to prevent algae proliferation inside by sunlight entering through the acrylic material. The filtration rate of continuous filters was 1.69 ± 0.01 $m^3.m^{-2}.day^{-1}$ for C-HSSF1 and 0.97 ± 0.96 $m^3.m^{-2}.day^{-1}$ for C-HSSF2. On the other hand, the I-HSSF hydraulic head was variable and, consequently, the filtration rate as well. The maximum filtration rate of I-HSSF1 was 3.2 $m^3.m^{-2}.day^{-1}$ shortly after feeding and decreased to zero and the maximum filtration rate of I-HSSF2 was 3.94 $m^3.m^{-2}.day^{-1}$. The filters had a daily production of 48 L each.

2.1.2 Physical characterization of materials

The thickness of the water layers (top of fine sand), fine sand, coarse sand, fine gravel and coarse gravel, respectively, were 10 cm, 50 cm, 5 cm, 5 cm and 7.5 cm. The fine sand had an equivalent diameter of 0.17 mm (D_{10}), a uniformity coefficient of 1.73 average particle diameter of 2.70 $x10^{-4}$ m. The physical parameters used in the study, such as: the thickness of the layers, granulometry, specific mass, the void index and the permeability were the same for the four filters and the standards used in the tests are contained in the supplementary material.

2.1.3 Experimental RTD

The disturbance chosen for C-HSSFs and I-HSSFs was of the step type, as reported by Maciel and Sabogal-Paz (2020), Terin and Sabogal-Paz (2019) and Sabogal-Paz et al (2020).

Tracer tests on each of the filters were performed in triplicate with a sodium chloride solution with a concentration of 100 $mg.L^{-1}$. The variation in the electrical conductivity of the filtered water was measured at the filter outlet, in real time, with a conductivity probe from Venier Software & Technology, USA.

The conductivity probe was positioned at the outlet of the tap and inside a bottle. This bottle made it possible to read the samples as the treated water that came out through the tap was collected and temporarily stored in that bottle and renewed each time a new sample of treated water was received.

The calibration of the probe allowed to correlate the variation in conductivity with the concentration of the tracer. The probe was connected to a computer with the Logger Lite software (Venier Software & Technology, USA) that allowed us to collect and store the data of the measurements of the tracer concentration over time. The dynamic response time of the conductivity probe was 5 seconds and the data were measured every 60 s in the treated water that was collected at the filter outlet.

Data processing was performed using Excel 2013 software (Microsoft®, USA) and OriginPro 8 software (OriginLab, USA). The concentration versus time curve was normalized to obtain the F curve and then derived to obtain the E curve. After each test, the filters were cleaned by introducing tap water until the tracer was completely eliminated.

In the C-HSSFs, the tracer tests were performed with the same filtration rate used during the operation of the filters. The procedure resulted in the concentration versus time curve (C vs. t). These experimental curves were adjusted based on the three mathematical models of dispersion: model of continuous mixing tank reactors (N-CSTRs) and the models of low and high dispersion, as reported by Levenspiel (1999).

In the I-HSSFs tracer tests, the disturbance was performed with the first feeding with 100 $mg.L^{-1}$ salt solution and then with tap water until the tracer concentration was close to zero. The filtration rate decreased to zero when the hydraulic load reached the minimum water level, at which time new feeding was performed. The volume of each

feed corresponded to the volume of voids in the filter. In total, four 10 L feeds were used in I-HSSF1 and four 15 L feeds in I-HSSF2.

Afterwards, the Modified Morris Dispersion Index (MMDI) proposed by Lynn et al. (2013) was calculated, which is a modification of the Morrill Dispersion Index (MDI) according to Tchobanoglous et al. (2003). The MDI index ranges from 1.0 (ideal piston flow reactors - PFR) to 22 (ideal complete mix reactors - CSTR) according to Tchobanoglous et al. (2003).

The theoretical RTD was calculated considering the ratio between the volume of water stored by C-HSSF1 and C-HSSF2 of 10L and 15L, respectively, and the daily flow of 48 L for both.

2.2. Mathematical modelling and simulation of HSSFs

The simulations of the HSSFs solved the mass conservation and momentum conservation equations using the ANSYS Fluent software (version 2020 R2) based on the finite volume method, where the differential equations are integrated in each mesh control volume, generating a set of discrete algebraic equations. The resulting linear system was then solved numerically in an iterative way until the solution was reached with previously determined precision.

The three-dimensional equations of the conservation of mass and amount of movement are given by Eq. 1 (all domains - continuity equation) and Eq. 2 (fluid domain - Navier-Stokes equation) (Navier, 1823; Stokes, 1845). In the filtering and support layers of the HSSFs, the term source of moment (S_i) was added to the fluid flow equations in Eq. 3 (Porous Domain, simple homogeneous porous media of Darcy-Forchheimer Equation) (Darcy, 1856; Forchheimer, 1901a, 1901b). The term source of moment consists of two parts: loss of viscosity (i.e., Darcy's Law in porous media, the

first term on the right side of Eq. 3), and inertial loss (i.e., the second term on the right side of Eq. 3).

$$\nabla \cdot (\rho u) = 0 \tag{1}$$

$$\nabla \cdot (\rho u u) = -\nabla \mathrm{p} + \nabla \cdot \left(\mu \left(\nabla \mathrm{u} + \nabla u^{T} \right) - \frac{2}{3} \delta \nabla . u \right) \tag{2}$$

$$S_i = -\left(\frac{\mu}{\alpha} u_i + C_2 \frac{1}{2} \rho |u| u_i \right) \tag{3}$$

Where, $u \in \mathbb{R}^3$ is the velocity vector; ρ is the density of the fluid (water) [kg.m^{-3}]; p is the pressure [atm]; μ is the viscosity [m^2.s^{-1}]; where, S_i is the source term for *i* in (*x*, *y* or *z*) in the moment equation, α is the permeability of the porous medium [cm.s^{-1}], $|u|$ is the magnitude of the velocity [m.s^{-1}], and D and C are the diagonal matrices with $1/\alpha$ and C_2, respectively.

Eq. 3 contributes to the pressure gradient in the porous cell, creating a pressure reduction that is proportional to the velocity of the fluid in the cell (ANSYS, 2013). The parameters of viscous resistance (1/α) and inertial resistance (C_2) used for porous media are calculated by Eq. 4 and Eq. 5 of the Ergun Equation (Ergun, 1952).

$$\alpha = \frac{D_p^2}{150} \cdot \frac{\varepsilon^3}{(1-\varepsilon)^2} \tag{4}$$

$$C_2 = \frac{3{,}5}{D_p} \cdot \frac{(1-\varepsilon)}{\varepsilon^3} \tag{5}$$

Where: 1/α – Viscous resistance [m^{-2}]; D_p - Average particle diameter [m]; ε – Index of voids [$kg.m^{-3}.kg^{-1}.m^3$]; C_2 – Inertial resistance [m^{-1}]; ε – Fraction of voids [$kg.m^{-3}.kg^{-1}.m^3$].

In laminar flows through porous media, the pressure drop is typically proportional to the velocity and the constant C_2 can be considered zero (ANSYS, 2013). Ignoring convective acceleration and diffusion, the middle model is reduced to Darcy's Law (Darcy, 1856), according to Eq. 6.

(6)

$$\nabla p = -\frac{\mu}{\alpha} u$$

Inertial losses in a porous medium, at high flow velocities, can be corrected by the constant C_2 of Eq. 3. This constant can be seen as a loss coefficient per unit length along the flow direction, thus allowing the drop of pressure, specified as a function.

If the permeability term can be eliminated, only the term of inertial loss can be used, producing the simplified form of the porous medium equation (Eq. 3) by Eq. 7 in the x, y and z directions (ANSYS, 2013).

(7)

$$\nabla \mathrm{p} = -\sum_{j=1}^{3} C_{2_{ij}} \left(\frac{1}{2} \rho \, \boldsymbol{u}|\boldsymbol{u}|\right)$$

The physical domain to be studied in the HSSFs is delineated by the walls of the filter and its interior, composed of layers of water, filter material and the support layer. The physical properties of the constituent materials of the physical domain, such as viscosity, specific mass, pressure, porosity and hydraulic conductivity (or permeability), were obtained in laboratory tests (supplementary material). The viscosity used was 1.003 x 10^{-3} $kg.m^{-1}.s^{-1}$ and the density was 9.982 x 10^2 $kg.m^{-3}$.

Thus, the boundary conditions of entry and exit were established for each of the constituent layers of the HSSF and the behaviour of the solution of the equations as a function of time was specified.

The CFD simulation was developed using Ansys 2020 R2 software from Ansys® and its subcomponents and a model was generated for each filter. Initially, the geometry of each HSSF was created using Autodesk® AutoCAD 2010®, and then the mesh was generated using Ansys 2020 R2 Meshing (Ansys®) with different refines. Then, the control conditions were defined to run the simulation in Ansys 2020 R2 Fluent (Ansys®) and the results were visualized in Ansys 2020 R2 CFD Post (Ansys®).

The models were simulated on a computer with an Intel® Core ™ i7-7500U CPU @ 2.70 GHz 2.90 GHz, 64-bit operating system, 8 GB installed memory (RAM), 1 TB HD, operating on Microsoft's Windows 10 platform ®.

The results generated the velocity profiles and the flow current lines inside the filters. At the end of the simulation, the verification and validation of the mathematical models were performed based on the results obtained in the experimental tracer tests.

In the present study, two simulations were carried out for each HSSF: the first of the flow, which was carried out in a permanent regime; and the second from RTD, performed in a transient regime (passive scalar).

In the four mathematical models of the HSSFs, to facilitate modelling, the following criteria were adopted: i) single-phase flow in three dimensions; ii) Newtonian fluid at steady state; iii) isothermal flow, laminar flow, incompressible flow and flow in porous medium in the filtering and draining layers; and iv) homogeneous and specific porosity and permeability for each of the filtering and draining layers; as reported by Berbert et al. (2016).

The boundary conditions used for the permanent regime, Navier-Stokes, were: i) Inlet: prescribed velocity; ii) Outlet: prescribed pressure; iii) Wall condition: non-slip. The boundary conditions for the transient, passive scalar regime were: i) Inlet: prescribed concentration of 100; ii) Outlet: null gradient; iii) Wall condition: impermeable (null normal gradient).

The boundary conditions used for the permanent regime, Navier-Stokes, were: i) Inlet: prescribed velocity; ii) Outlet: prescribed pressure; iii) Wall condition: non-slip. The boundary conditions for the transient regime, passive scalar, were: i) Inlet: prescribed concentration of 100; ii) Outlet: null gradient; iii) Wall condition: impermeable (null normal gradient).

In Figure 1, the inlet, outlet and wall of the filter are indicated. The fluid velocity at the entrance of the C-HSSFs was calculated by the ratio between the flow (48 $L.day^{-1}$) and the area of the entrance section.

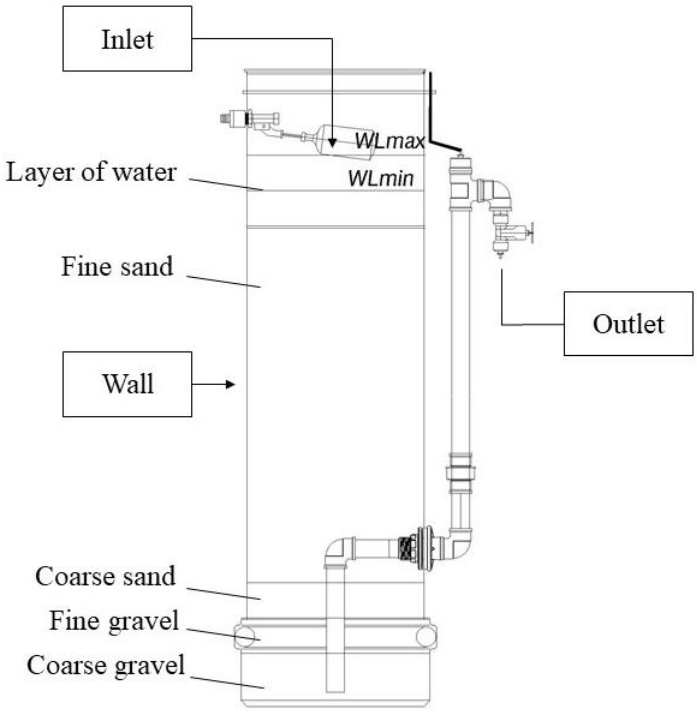

Figure 1. Schematic of the C-HSSFs indicating the inlet, the outlet and the filter wall for modelling purposes

In the I-HSSFs, the fluid velocity at the inlet was obtained from the average velocity calculated in the RTD experimental test. The average flow was obtained by the ratio between the volume of water and the total time of this test and then the velocity was calculated by the ratio between this flow and the area of the inlet section.

A time step was selected that guaranteed a Courant Number (Co) or CFL criterion (Courant, Friedrichs and Lewy, 1967), less than 1, according to Eq. 8.

(8)

$$Co = \frac{U \,.\, \Delta t}{\Delta}$$

Where parameter U is the local velocity [m.s^{-1}], Δt is the time step [s] and Δ is the local length scale characteristic of the finite volumes of the mesh [m].

The Courant Number is a local parameter of the fluid, dimensionless domain, which represents the ratio between the characteristic physical time for the information to propagate the U velocity from one node in the mesh to the next, and the discrete time step used in the simulation. The use of longer time steps (Co> 1) locally implies a violation of the transport physics of the property under analysis, which almost always results in numerical oscillations and/or divergence of the numerical solution.

After constructing the meshes with different refines (variation in the number of finite elements), a mesh independence test was carried out. In this test, the velocity obtained for each mesh was analysed to determine from which degree of refinement the calculated values for velocity became independent of the mesh. Therefore, the minimum volume of the finite element (ΔV [m^3]) was obtained from the meshes generated in the CFD, adopting the Courant Number (Co) of 0.9, according to Eq. 8 and Eq. 9.

(9)

$$\Delta = \sqrt[3]{min(\Delta V)}$$

The condition used to verify the independence of the mesh was that the velocity in the filter outlet, located at the centroid of the end of the outlet tube, did not present variations greater than 5% of the real velocity.

2.2.1 Numerical method

Two geometries were created corresponding to each filter diameter (190 mm and 250 mm) and it is not necessary to construct four geometries (one per filter), since the flow characteristic (continuous or intermittent) depends only on the boundary conditions inserted in the simulation. The elaborated geometries followed the structure shown in Figure 1.

Table 1 shows the numerical parameters used to simulate the filters and the RTD simulations. The reference pressure adopted was 1 atm and the relative static pressure was 0 atm, considering that the experiment was carried out close to sea level and the flow was free. In the simulations carried out in a transient regime, that is, in the RTD simulations, the following solution methods were used: i) Transient formulation of "first implicit order", ii) SIMPLE coupling scheme.

Table 1 – Numerical parameters for filter simulation and RTDs simulation

Parameters	**C-HSSF1**	**C-HSSF2**	**I-HSSF1**	**I-HSSF2**
Reference pressure [atm.]	1	1	1	1
Relative static pressure [atm.]	0	0	0	0
Entrance section area [m^2]	0.0283	0.0491	0.0283	0.0491
Inlet fluid velocity [$m.s^{-1}$]	1.96×10^{-5}	1.13×10^{-5}	4.10×10^{-5}	5.66×10^{-5}
Relative outlet pressure [atm.]	0	0	0	0
Passive scalar value	100	100	100 0	100 0

Time step (s)	23		56		600		600	
Number of time steps	1566		1072	13	30	12	24	
Maximum number of iterations	15		15	15		15		
Total computational time (h)	5		8	4		4		

Notes: C-HSSF1 - continuous filter with a diameter of 190 mm; C-HSSF2: continuous filter with a diameter of 250 mm; I-HSSF1: intermittent filter with a diameter of 190 mm; and I-HSSF2: intermittent filter with a diameter of 250 mm.

In I-HSSF1, a volume of 30 L was used in a time of 430 min and in I-HSSF2, 60 L was applied in 360 min, obtained in the experimental tracer tests. The relative pressure at the outlet of 0 atm was used, as the flow depended only on the variation of the water level that preceded the layer of fine sand, that is, the flow was free.

The calculated values of viscous resistance ($1/\alpha$) and inertial resistance (C_2) were obtained based on the mean particle diameter ((D_p) and the void index (ε) values obtained in a laboratory test are contained in the supplementary material.

In the simulations carried out in the HSSFs steady state, the following solution methods were used: i) Pressure-velocity coupling scheme: SIMPLE (Semi-Implicit Method for Pressure Linked Equations); ii) spatial discretization of gradient "cells based on least squares"; iii) "second order" pressure spatial discretization; and iv) spatial discretization of "second-order upwind" momentum. The computational time for each of the simulations was approximately 2 hours and 400 iterations were used. The results of the simulations residues were less than $1x10^{-5}$.

The dead zones were quantified by occupied volumes between velocities greater than 0 and less than $1.05x10^{-5}$ $m.s^{-1}$ for C-HSSF1, $6.90x10^{-6}$ $m.s^{-1}$ for C-HSSF2, $2.32x10^{-5}$ $m.s^{-1}$ for the I-HSSF1 and $2.22x10^{-5}$ $m.s^{-1}$ for the I-HSSF2. These velocities

were determined punctually in the velocity contour plane where there was no formation of current lines. After defining this criterion and delineating the dead zone, its volume can be calculated in relation to the sum of the volumes of the filtering and draining layers. The images of the current lines and the velocity contour plane are shown in the supplementary material.

2.2.2 RTD simulation

The determination of the residence time distribution with CFD used the passive scalar equation (TALVY et al., 2011) for a transient regime as a solution for using a tracer concentration in the model.

The transport of a passive scalar refers to the convection-diffusion of a scalar field within the fluid in motion without significant changes in the properties of the fluid under analysis, such as in the velocity field, pressure and temperature, hence the term passive. Eq. 10 was used to calculate the passive scalar, and thus solve the tracer test in the model (ANSYS, 2013).

$$\frac{\partial \rho\, C}{\partial t} + \nabla.(\rho \mathrm{UC}) = \nabla.\left(\mathrm{D}_{disp} \nabla \mathrm{C}\right) \quad (10)$$

Where: ρ is the density of the fluid in $kg.m^{-3}$; C is the tracer concentration in $mg.L^{-1}$; U is the velocity vector in $m.s^{-1}$; and D_{disp} is the dispersion coefficient given in $m^2.s^{-1}$.

In this equation, the first term on the left side of the equality corresponds to the concentration of solute in the solvent over time, the second term corresponds to the advective term of concentration carried by the velocity field; and the one on the right side of equality, the term corresponds to the diffusive term of concentration.

The ANSYS Fluent software solves the transport equation for a passive scalar defined by the user as User-defined scalar (UDS) in the same way as it solves the

transport equation for a scalar such as mass fraction (ANSYS, 2013). For transient simulations, the governing equations were discretized in space and time.

In the CFD tracer test, the diffusion coefficient at 25 ° C of NaCl corresponding to $1.612x10^{-9}$ $m^2.s^{-1}$ with diffusivity of $1.609x10^{-6}$ $kg.m^{-1}.s^{-1}$ was used, as established by Robinson and Stoke (1955). In the tests of C-HSSFs and I-HSSFs, the dimensionless scalar value of 100 was used to refer to the 100 $mg.L^{-1}$ salt solution and 0 for the other tap water feeds. The outgoing concentration of the passive scalar was obtained by the integral of the outgoing section area.

2.3. Model validation and verification

Furman & Stegowski (2011) suggested the following steps to verify the CFD results: i) Choose the CFD model appropriately from the physical point of view of the problem; ii) obtain the velocity field and the RTD simulation with CFD; iii) evaluate the deviation of the results of the experimental RTD and RTD predicted with CFD; and iv) analyse the velocity fields if they are different simulated geometries.

The article presents the flow simulations applied in HSSFs using the Ansys Fluent 2020 R2 to analyse the influence of continuous (C-HSSF) and intermittent (I-HSSF) feeds and geometric shape changes on the hydrodynamic behaviour of the filter.

2.4. Statistical analysis

A priori the data sets were assessed for normality by the Shapiro-Wilk test, which allowed us to classify each data set as: data with normal distribution (Shapiro-Wilk test $p > 0.05$) in which parametric tests are applied or data with non-normal distribution (Shapiro-Wilk test $p < 0.05$) in which non-parametric tests are applied.

The statistical analysis used to validate experimental and computational RTD tests was performed using the Kruskal-Wallis non-parametric test (95% confidence limit) followed by the Mann-Whitney pairwise test, indicated when comparing three or more groups, to perform the tests, the free access software PAST 4.03 (PAlaeontological STatistics) was used.

3. Results and discussion

3.1. Numerical Results

In steady state simulations, the outlet velocities were obtained, located in the centre of the outlet tube, that is, in the centroid of the end of the outlet tube. The behaviour of this velocity was analysed as a function of the control volumes, as shown in Figure 2. It can be seen that the minimum value required for variations not greater than 5% for the C-HSSF1 was 233,264 elements (Figure 3A) and for C-HSSF2 it was 268,474 elements (Figure 3B).

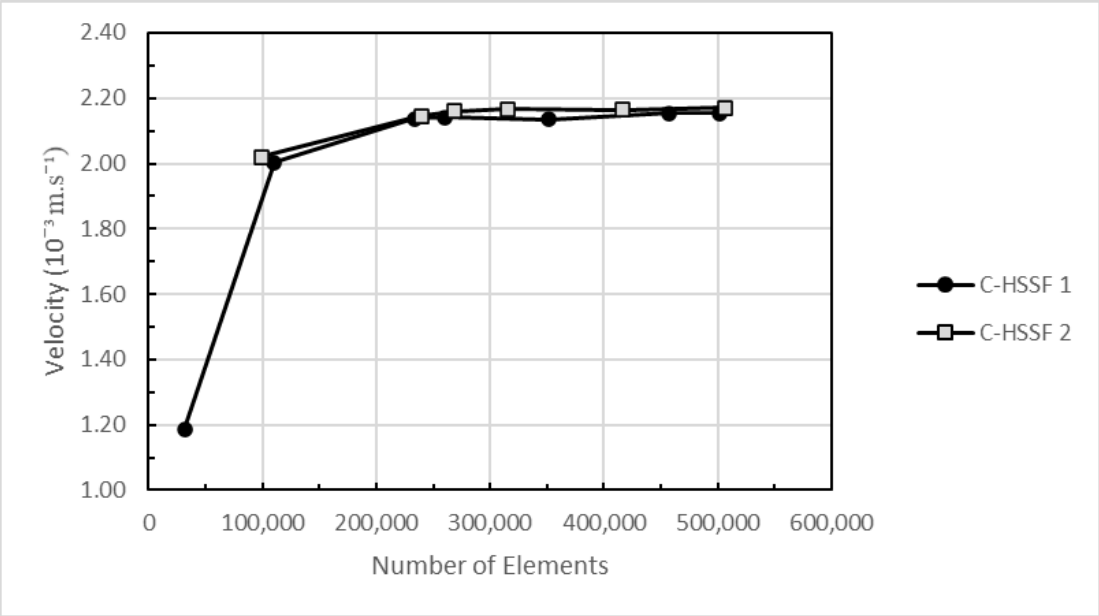

Figure 2 – Velocity as a function of the number of elements of the numerical grid obtained in the mesh independence test of C-HSSF1 and C-HSSF2 using Ansys® Software 19.2.

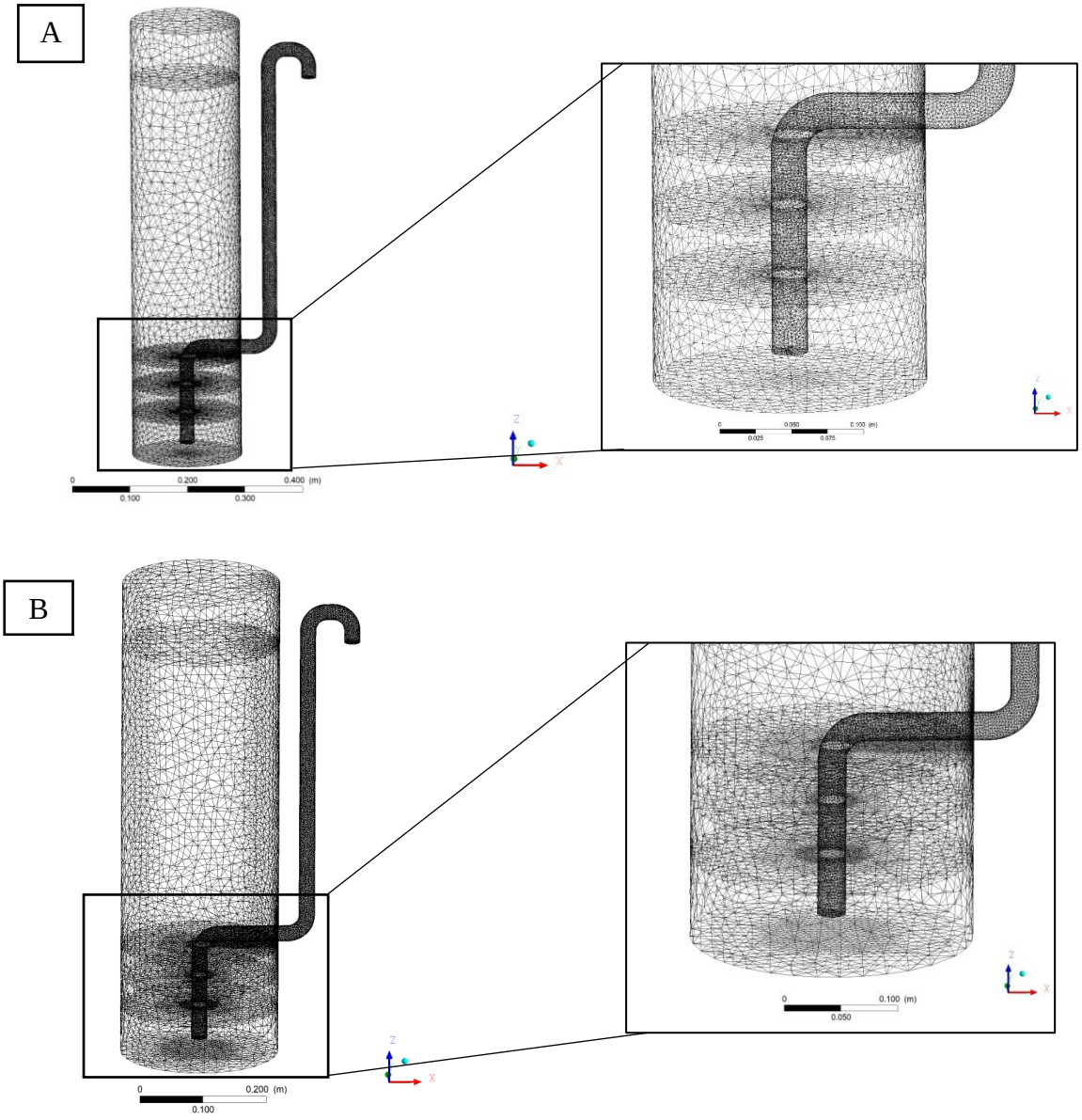

Figure 3 – Meshes obtained for C-HSSF1 and C-HSSF2.

Legend: Figure 3A (C-HSSF1 with 233,264 elements of tetrahedral type); and Figure 3B (C-HSSF2 with 268,474 elements of tetrahedral type).

According to the results, the current lines showed symmetry in relation to the central axis, the existence of a dead zone near the base of the HSSF in the coarse gravel layer and the absence of a short circuit. Similar behaviour was described by Berbert et al. (2016) who found the symmetry and dead zone in HSSF, without obtaining the volume of the dead zone, with the same output configuration used in the present study.

In the simulated HSSFs, the locations of the dead zone were defined, and the volumes were obtained. The percentage results of the volume of the dead zones in relation to the sum of the volumes of the filtering and draining layers were: C-HSSF1 2.19%, C-HSSF2 2.99%, I-HSSF1 2.37% and I-HSSF2 2.60%. It was found that the values were low, below 3%, and the behaviour of the current lines in the HSSFs were similar, regardless of the geometry or type of flow. It was also found that for the same type of flow regime, whether in continuous or intermittent flow, the increase in diameter implied an increase in the volume of the dead zone. The results of the dead zone volumes are shown in the supplementary material.

The velocity profiles in the XZ plane at the centre of the HSSFs were visually similar, as seen in Figure 4. The velocity scale was previously defined, and the outlet tube was removed from the visualization for a better analysis of the velocity variation inside the filters. It was found that in the water layer the velocity was higher than when it reached the filtering and draining layers, and then increased in the coarse gravel layer before reaching the water outlet.

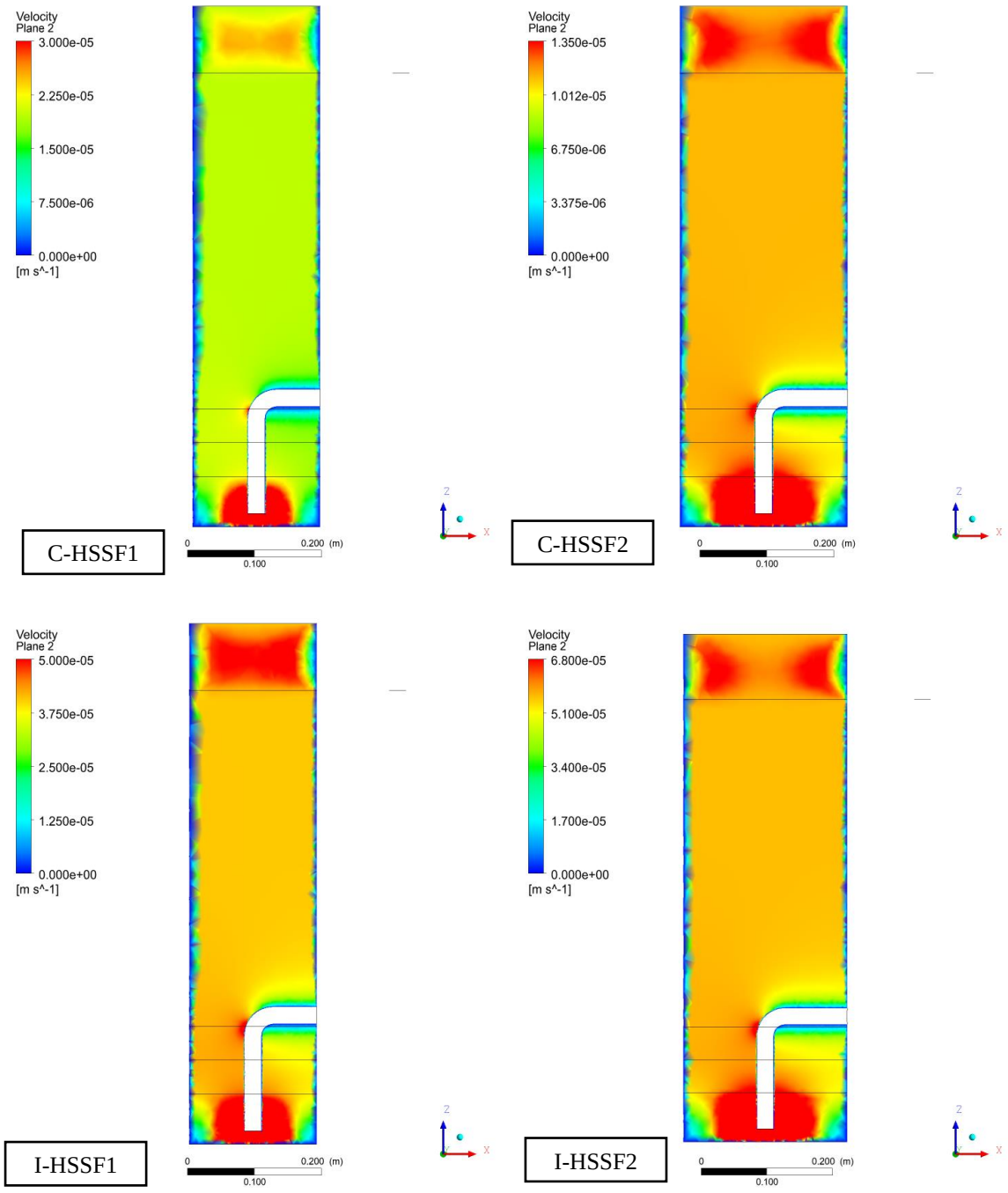

Figure 4 – Velocity profiles on the XZ plane located in the center of the HSSFs indicating the maximum and minimum velocities

In the simulations, the velocities were sampled in the centroid of the filter, located in the layer of fine sand, and the velocities of the real experiments were

compatible (Table 2), which indicates the representativeness of the mathematical models in relation to the HSSFs built in real scale.

Table 2 - Velocity of experimental and simulated HSSFs

HSSF	Velocity ($m.s^{-1}$)		Difference (%)
	Experimental	Simulation	
C-HSSF1	$1.959x10^{-5}$	$1.956x10^{-5}$	-0.15
C-HSSF2	$1.132x10^{-5}$	$1.129x10^{-5}$	-0.27
I-HSSF1	$4.10x10^{-5}$	$4.092x10^{-5}$	-2.44
I-HSSF2	$5.66x10^{-5}$	$5.648x10^{-5}$	-2.83

The velocity profiles obtained for the HSSFs, as shown in Figure 5, show that at the initial points on the water slide the velocity is higher and then there is a reduction when it starts to percolate through the filter layer. The velocity remains constant until reaching the last layers, when there is an increase close to the water outlet/treated water collection region and the last point shows the velocity close to the wall at the bottom of the filter. The increase in velocity near the water outlet corroborates the observations of Berbert et al. (2016).

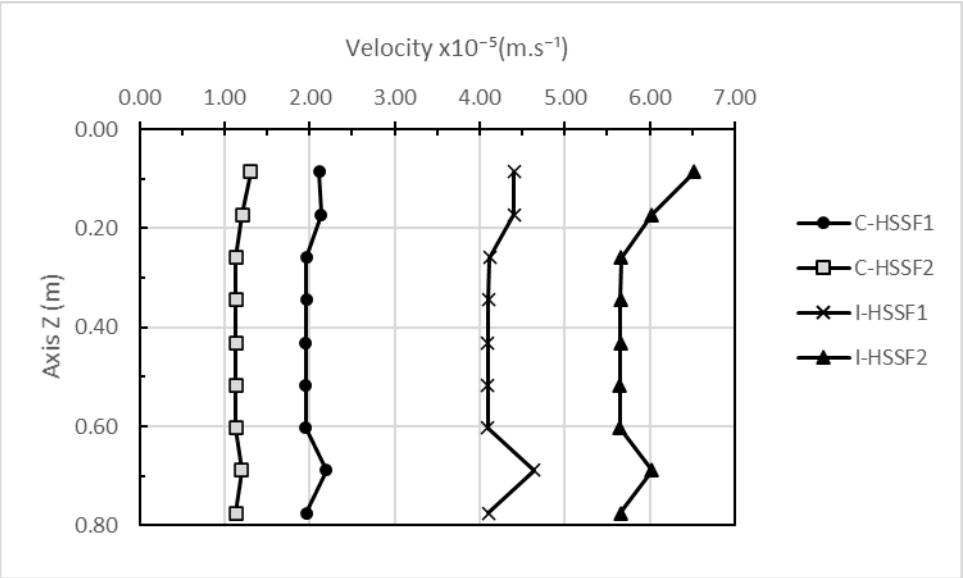

Figure 5 – Velocity profiles of HSSFs.

The analysis of Figures 4 and 5 allows us to highlight two important points. The first point shows that despite the velocity profiles being visually similar, as can be seen in Figure 4, it is observed in Figure 5 that the I-HSSFs present a greater velocity variation than the C-HSSFs at the beginning of the filtering layer. This characteristic can negatively affect the development of the biological layer, which needs an environment in balance for its development and, consequently, reduce the treatment efficiency in filters operated in intermittent flow. The second point shows that this velocity variation is still greater in the C-HSSFs near the base and the outlet collector tube, which indicates that each of the filters needs an individual determination of the limiting velocity to define the dead zone, or that is, the same dead zone delineated velocity cannot be used for the four filters.

3.2. Comparison between experimental and simulated RTD (CFD)

534 Table 2 shows that the velocities obtained in the simulation were close to and
535 below the experimental velocities and the analysis of the results obtained with the
536 experimental tracer tests and the CFD tracer test, presented in Figure 6, can classify the
537 HSSFs as a plug flow reactor.
538

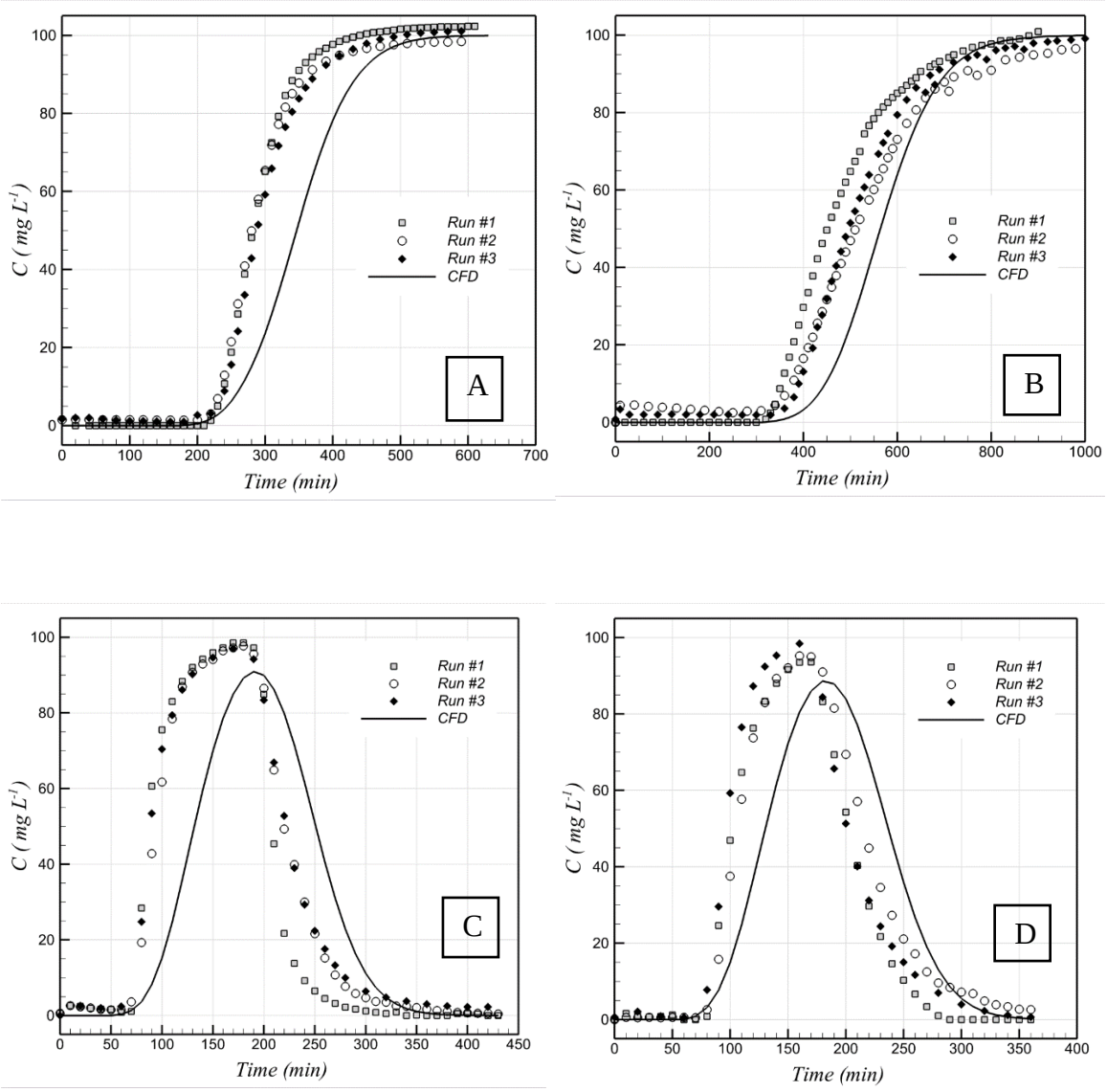

539 Figure 6 – Experimental and computational RTD of HSSFs.

540 Notes: A - C-HSSF1; B - C-HSSF2; C - I-HSSF1; and D - I-HSSF2.

541

The results obtained in the I-HSSFs corroborate the behaviours described by Andreoli and Sabogal-Paz (2020), Bradley et al. (2011), Elliott et al. (2008), Maciel and Sabogal-Paz (2020) and Terin and Sabogal-Paz (2019), who characterized the HSSF as a plug flow reactor.

According to the adaptation of the MDI to the mMDI proposed by Lynn et al. (2013), they presented mMDI results of 2.92. In the I-HSSFs of Andreoli and Sabogal-Paz (2020), the MDI values were 2.19 and 2.21 and the mMDI results were 2.47 and 2.56, respectively, and Sabogal-Paz et al. (2020) reported mMDI values of 0.95. In the study, the results of the mMDI for I-HSSF 1 were 2.22 ± 0.132 and for I-HSSF 2, it was 2.04 ± 0.082, which is close to the results obtained by Andreoli and Sabogal-Paz (2020).

The residence time distribution for C-HSSF 1 was 293 ± 6 min and for C-HSSF 2, it was 462 ± 79 min. These values are close to the theoretical residence time distribution of 300 ± 8 min and 450 ± 13 min for C-HSSF1 and C-HSSF2, respectively. The adjustment data for the N-CSTR model and for the models with small and large dispersion of the C-HSSFs are shown in Table 3. In the C-HSSF 1 (cross-sectional area = 0.028 m^2), the N-CSTR model presented the best result, requiring 22 complete mix reactors in series. The largest number of reactors in series indicates a plug flow reactor (Levenspiel, 1999). The C-HSSFs studied by Sabogal-Paz et al. (2020) presented N = 17 (filter cross-section of 0.0075 m^2). Those tested by Andreoli and Sabogal-Paz (2020) obtained N = 8 and N = 13 (filter cross-sectional area of 0.049 m^2) and those tested by Terin and Sabogal-Paz (2019) had N = 6 (filter cross-sectional area of 0.049 m^2). In the C-HSSF 2, the piston model with great dispersion had the best result. Although C-HSSF1 and C-HSSF 2 fit different models, the results of both refer to a plug flow reactor.

Table 3 - Tracer test results for the C-HSSF

HSSF	Statistic	N-CSTR		Small dispersion model		High dispersion model	
		N	r^2	$D.\mu L^{-1}$	r^2	$D.\mu L^{-1}$	r^2
C-HSSF1	Mean	22	0.86	0.02	0.82	0.02	0.80
	Standard deviation	6	0.05	0.01	0.04	0.01	0.03
C-HSSF2	Mean	10	0.64	0.05	0.63	0.05	0.68
	Standard deviation	2	0.14	0.01	0.10	0.01	0.07

The flow in piston flow observed in I-HSSFs and C-HSSFs is good because it shows that the treatment will be homogeneous in all water fractions that enter the filter. Sabogal-Paz et al. (2020) suggested that the piston flow reactor improved the development of the biological layer and the efficiency of the treatment.

Figure 6 shows the comparison between experimental and simulated RTD for C-HSSFs and I-HSSFs. Results from CFD simulations are validated with experimental RTD tests (Brannock et al., 2010; Furman & Stegowski, 2011; Gharibian et al., 2020; Klusener et al., 2007; Qi et al., 2013; Talvy et al., 2011; Zhang et al., 2007). The computational RTDs of the I-HSSF1 and I-HSSF2 show that the simulations present a perfect Gaussian distribution, as expected for the simulation.

The form of data collection may have influenced the signal obtained experimentally, which shows the difference observed in the results of the experimental and simulated RTDs, as was found by Talvy et al. (2011) who chose to modify the simulated RTD to fit the experimental RTD. It is noteworthy that the RTDs were

583 simulated using the average velocity and constant values of the boundary condition,
584 such as porosity and permeability. When the real experiment was constructed, the layers
585 may have undergone natural and anthropic compaction, accommodating the grains
586 during assembly and feeding, and presented values different from those obtained in the
587 laboratory, which may explain the delay in the response time to the stimulus of the
588 simulated HSSFs compared to the experimental ones.

589 The Kruskal Wallis non-parametric test (5% significance level) showed that the
590 results of the three experimental tests of the RTDs and the computational test of the
591 RTD did not show statistically significant differences between each other for each of the
592 filters. The C-FLD 1, C-FLD 2, I-FLD 1 and I-FLD2 had a p-value of 0.27; 0.25; 0.01
593 and 0.38. Thus, the RTD result obtained with CFD is like the results of RTDs obtained
594 experimentally in full-scale physical models, as there was no significant difference
595 between the results.

596 The numerical simulations of the RTDs were validated with the experimental
597 tests of the RTDs, and therefore the hydrodynamics of the HSSFs were analysed. The
598 behaviour of the current lines of the C-FLDs and I-FLDs were similar and showed that
599 they are not influenced due to the geometry, the filtration rate, or the type of continuous
600 or intermittent feeding. In the C-FLDs and I-FLDs, it was found that the flow was of the
601 piston type, with no short circuit and having a dead zone close to the base. The smaller
602 the diameter, the smaller the dead zone. The C-HSSFs showed minimization adverse
603 hydraulic phenomena, as seen by the lower variation of the filter velocity profile, which
604 may reflect in the improvement of treatment efficiency due to the reduction of
605 interferences in the development of the biological layer.

606

607 **4. Conclusions**

The behaviour of the C-HSSFs and I-HSSFs flow lines were similar according to the visual analysis of the 3D flow lines (supplementary material). In the C-HSSFs and I-HSSFs, it was found that the flow was of the piston type, with no short circuit and having a dead zone close to the base. The piston flow is good for the treatment because the incoming water will be treated at the same time in all its portions, favouring the efficiency of the HSSF.

The flow of the piston type is desirable for HSSFs, as it allows biological treatment to occur at the beginning of the filter layer and, concomitantly, physical-chemical treatments occur as the water percolates through the filter layer until the treated water is obtained at the end of layers, that is, the incoming water will be treated at the same time in all its portions as it percolates through the filter media.

The volumes of the dead zone in the HSSFs were less than 3%, and due to this low value, there was no need to change the design of the HSSFs. The statistical results showed that there were no significant differences in the statistical comparison of the data from the experimental and simulated RTDs.

In view of this and considering that all filters showed flow of the piston type, the choice of geometry and type of feed depends on studies of the analysis of treatment efficiency considering the water quality parameters.

Acknowledgements

This work was supported by the Global Challenges Research Fund (GCRF) UK Research and Innovation (SAFEWATER; EPSRC Grant Reference EP/P032427/1).

Statement

The authors hereby declare previous originality check, no conflict of interest and open access to the repository of data used in this paper for scientific purposes.

Supplementary Material

Brazilian standards used in the physical characterization of materials and experimental results are provided as supplementary material.

References

Andreoli, F. C., Sabogal-Paz, L. P., 2020. Household slow sand filter to treat groundwater with microbiological risks in rural communities. Water Research. 186, 116352. https://doi.org/10.1016/j.watres.2020.116352.

ANSYS, Inc., Ansys fluent User's Guide, 2013. Release 15.0, ANSYS, Canonsburg, United States of América.

Berbert, A. C., Almeida, R. A de, Rezende, R. V. de P., Lautenschlager, S. R. The use of computation fluids dynamics to select outlet system configuration in biosand filters. Conference: 13th IWA Specialized Conference on Small Water and Wastewater Systems & 5th IWA Specialized Conference on Resources-Oriented Sanitation At: Athens, September, 2016.

Botari, A., Di Bernardo, L., 2012. Hydrodynamic analysis of particle collection efficiency: comparing downflow and upflow filtration. Acta Scientiarum. Technology, v. 34, n. 2, p. 167-175. doi:10.4025/actascitechnol.v34i2.10803.

Brannock, M., Wang, Y., Leslie, G., 2010. Mixing characterisation of full-scale membrane bioreactors: CFD modelling with experimental validation. Water Research 44 (10), 3181–3191. https://doi.org/10.1016/j.watres.2010.02.029.

Bradley, I., Straub, A., Maraccini, P., Markazi, S., Nguyen, T.H., 2011. Iron oxide amended biosand filters for virus removal. Water Res 45, 4501–4510. doi:10.1016/j.watres.2011.05.045.

Campos, L.C., Smith, S.R., Graham, N.J.D, 2006a. Deterministic based model of slow sand filtration. I: model development. Journal of Environmental Engineering 132(8), 872-886. https://doi.org/10.1061/(ASCE)0733-9372(2006)132:8(872).

Campos, L.C., Smith, S.R., Graham, N.J.D, 2006b. Deterministic based model of slow sand filtration. II: model application. Journal of Environmental Engineering 132(8), 887-894. https://doi.org/10.1061/(ASCE)0733-9372(2006)132:8(887).

CAWST, 2012. Biosand Filter Construction Manual. Centre for affordable water and sanitation. Canada, Calgary.

CAWST, 2009. Biosand filter manual: Design, construction, installation, operation and maintenance, Canada, Calgary, Canada.

Courant, R., K. Friedrichs e H. Lewy. On the Partial Difference Equations of Mathematics Physics. IBM Journal, n. March, p. 215-234. 1967.

Dadonaite, B., Ritchie, H., Roser, M., 2020. Diarrheal diseases. Published online at OurWorldInData.org. (https://ourworldindata.org/diarrheal-diseases, accessed 19 May 2020).

Darcy, H. Les fontaines publiques de la ville de Dijon. Paris: Victor Dalmont, 1856. 647 p.

Elliott, M.A., Stauber, C.E., Koksal, F., DiGiano, F.A., Sobsey, M.D., 2008. Reductions of E. coli, echovirus type 12 and bacteriophages in an intermittently operated

household-scale slow sand filter. Water Res 42, 2662–2670. doi:10.1016/j.watres.2008.01.016.

Ergun, S. Fluid flow through packed columns. Chemical Engineering Progress, v. 48, n. 2, p. 89-94, 1952.

Forchheimer, P. Wasserbewegung durch Boden. Zeitschrift des Vereins Deutscher Ingenieure, v. 45, n. 49, p. 1736-1741, 1901a.

Forchheimer, P. Wasserbewegung durch Boden. Zeitschrift des Vereins Deutscher Ingenieure, v. 45, n. 50, p. 1781-1788, 1901b.

Furman, L., Stegowski, Z., 2011. CFD models of jet mixing and their validation by tracer experiments. Chemical Engineering and Processing: Process Intensification 50(3), 300–304. https://doi.org/10.1016/j.cep.2011.01.007.

Gharibian, S., Hazrati, H., Rostamizadeh, M. 2020. Continuous electrooxidation of Methylene Blue infilter press electrochemical flowcell: CFD simulation and RTD validation. Chemical Engineering & Processing: Process Intensification. 150 (2020) 107880. https://doi.org/10.1016/j.cep.2020.107880.

Jadhav, D., Husain, M., Chavan, F.I., 2015. Biosand Water Filter: A Boon. International Research Journal of Engineering and Technology 2 (3). https://www.irjet.net/archives/V2/i3/Irjet-v2i3262.pdf

Kennedy, T. J., Hernandez, E. A., Morse, A. N., Anderson, T. A. 2012. Hydraulic Loading Rate Effect on Removal Rates in a BioSand Filter: A Pilot Study of Three Conditions. Water, Air, & Soil Pollution, 223 (7), 4527-4537. https://link.springer.com/article/10.1007/s11270-012-1215-4.

Kikkawa, I. 2008. Modification of a Biosand Filter in the Northern Region of Ghana. Master of Engineering in Civil and Enviromental Engineering at the Massachusetts Institute of Techonlogy.

706 Klusener, P. A. A., Jonkers, G., During, F., Hollander, E. D., Schellekens, C. J.,
707 Ploemen, I. H. J., Othman, A., Bos, A. N. R., 2007. Horizontal cross-flow bubble
708 column reactors: CFD and validation by plant scale tracer experiments. Chemical
709 Engineering Science 62(18–20), 5495–5502.
710 https://doi.org/10.1016/j.ces.2007.03.044.
711 Langergraber, G., Giraldi, D., Mena, J., Meyer, D., Peña, M., Toscano, A., Brovelli, A.,
712 Korkusuz, E. A., 2009. Recent developments in numerical modelling of subsur-face
713 flow constructed wetlands. Science of The Total Environment 407 (13), 3931–3943.
714 https://doi.org/10.1016/j.scitotenv.2008.07.057.
715 Levenspiel, O., 1999. Chemical Reaction Engineering, Industrial & Engineering
716 Chemistry Research. https://doi.org/10.1021/ie990488g.
717 Lynn, T.J., Wanjugi, P., Harwood, V.J., Ergas, S.J., 2013. Dynamic performance of
718 biosand filters. J. Am. Water Works Assoc. 105 (10), E587–E595.
719 https://doi.org/10.5942/jawwa.2013.105.0116.
720 Maciel, P. M. F.; Sabogal-Paz, L. P. (2020). Household slow sand filters with and
721 without water level control: continuous and intermittent flow efficiencies.
722 Environmental Technology, 41(8), 944-958.
723 https://doi.org/10.1080/09593330.2018.1515988.
724 Navier, C. L. M. H. Mémoire sur les lois du mouvement des fluides. Mémoires de I'
725 Académie Royale des Sciences de I'Institut de France, v.6, p. 389-440, 1823.
726 Qi, W. K.; Guo, Y. L.; Xue, M.; LI, Y. Y. 2013. Hydraulic analysis of an upflow sand
727 filter: Tracer experiments, mathematical model and CFD computation. Chemical
728 Engineering Science. 104, 460-472. https://doi.org/10.1016/j.ces.2013.09.035.
729 Robinson, R. A.; Stoke, R. H. 1955. Electrolyte solutions.Butterworths Publications.
730 Londres.

731 Sabogal-Paz, L. P.; Campos, L. C.; Bogush, A.; Canales, M. 2020. Household slow
732 sand filters in intermittent and continuous flows to treat water containing low mineral
733 ion concentrations and Bisphenol A. Science of the Total Environment. 702, 135078.
734 https://doi.org/10.1016/j.scitotenv.2019.135078.
735 Sobsey, M.D., Stauber, C.E., Casanova, L.M., Brown, J.M., Elliot, M.A., 2008. Point of
736 use household drinking water filtration: a practical, effective solution for providing
737 sustained access to safe drinking water in the developing World. Environ. Sci.
738 Technol. 42, 4261e4267. https://doi.org/10.1021/es702746n.
739 Stokes, G. G. On the theories of internal friction of fluids in motion ando f the
740 equilibrium and motion of elastic solids. Transactions of the Cambridge
741 Philosophical Society, v. 8, p. 207-305, 1845.
742 Stropky, D.; Pougatch, K.; Nowak, P.; Salcudean, M.; Pagoria, P.; Gartshore, I.; Yuan,
743 J. 2007. RTD (residence time distribution) predictions in large mechanically aerated
744 lagoons. Water Science & Technology. 55, 11, 29-36.
745 https://doi.org/10.2166/wst.2007.346.
746 Talvy, S.; Debaste, F.; Martinelli, L.; Chauveheid, E.; HAUT, B. 2011. Development of
747 a tool, using CFD, for the assessment of the disinfection process by ozonation in
748 industrial scale drinking water treatment plants. Chemical Engineering Science. 66,
749 3185-3194. https://doi.org/10.1016/j.ces.2011.02.039.
750 Tchobanoglous, G., Burton, F.L., Stensel, H.D., 2003. Wastewater Engineering:
751 Treatment and Reuse. McGraw-Hill Higher Education, New York.
752 Terin, U. C.; Sabogal-Paz, L. P. 2019. Microcystis aeruginosa and microcystin-LR
753 removal by household slow sand filters operating in continuous and intermittent
754 flows. Water Research. 150, 29-39. https://doi.org/10.1016/j.watres.2018.11.055.

United Nations Environment Programme (UNEP). 2016. A Snapshot of the World's Water Quality: Towards a global assessment. Unites Nations Environment Programme, Nairóbi, Quénia.

YOUNG-ROJANSCHI, C.; MADRAMOOTOO, C. Comparing the performance of biosand filters operated with multiday residence periods. Journal of Water Supply: Research and Technology-Aqua. 64, 157. 2014a. https://doi.org/10.2166/aqua.2014.027.

YOUNG-ROJANSCHI, C; MADRAMOOTOO, C. Intermittent Versus Continuous Operation of Biosand Filters. Water Research v. 45. 1-10 p., 2014b

Zhang, L., Pan, Q., Rempel, G.L., 2007. Residence time distribution in a multistage agitated contactor with Newtonian fluids: CFD prediction and experimental validation. Industrial and Engineering Chemistry Research 46 (11), 3538-3546. https://doi.org/10.1021/ie060567+.

769 **Supplementary Material**

770

771 Table S1 – Standards used in the physical characterization of materials

Materials	Granulometry	CU[1]	Especific mass	Voids index	Permeability
Fine sand	ABNT NBR 11799/2016	ABNT NBR 6502/1995	ABNT NBR 6458/2016	ABNT NM 45/2006	ABNT NBR 13292/1995
Coarse sand	ABNT NM 248/2001				
Fine gravel					
Coarse gravel					

772 Notes: [1] Coefficient of uniformity (CU).

773

774 Table S2 – Specific mass, voids index and material of permeability

Materials	Specific mass ($g.cm^{-3}$)	Voids index	Permeability ($cm.s^{-1}$)
Fine sand	2.66	0.40	1.97×10^{-2}
Coarse sand	2.64	0.46	$1.06\ 10^{-1}$
Fine gravel	2.63	0.43	4.75
Coarse gravel	2.64	0.39	8.28

775

776 Table S3 - Characteristics of the porous media of the filters

Filter materials	D_p (m)	ε ( )	α (m^2)	1/α (m^{-2})	C_2 (m^{-1})
Fine sand	2.70×10^{-4}	0.40	8.64×10^{-11}	1.16×10^{10}	1.21×10^{5}
Coarse sand	1.30×10^{-3}	0.46	3.76×10^{-9}	2.66×10^{8}	1.49×10^{4}
Fine gravel	4.00×10^{-3}	0.43	2.61×10^{-8}	3.83×10^{7}	6.27×10^{3}
Coarse gravel	1.04×10^{-2}	0.39	1.15×10^{-7}	8.70×10^{6}	3.46×10^{3}

777 Notes: 1/α: viscous resistance, C_2: inertial resistance, D_p: average particle diameter, ε:

778 voids index

779

780

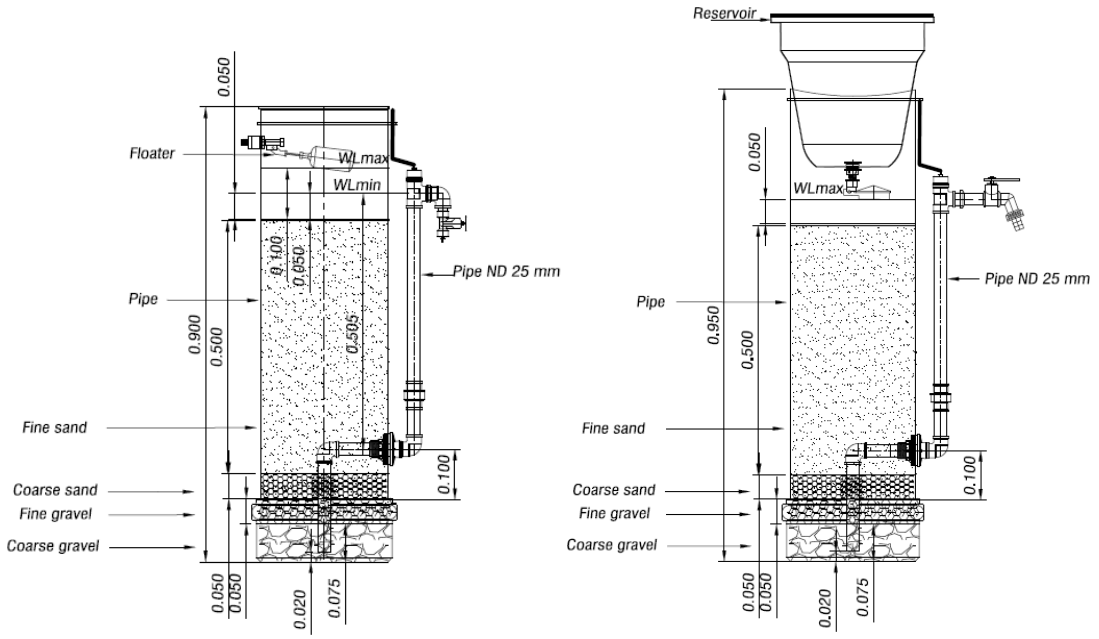

781

782 Continuous flow (C-HSSF) Intermittent flow (I-HSSF)

783 Figure S1. Scheme of the studied HSSFs (units in meters)

784

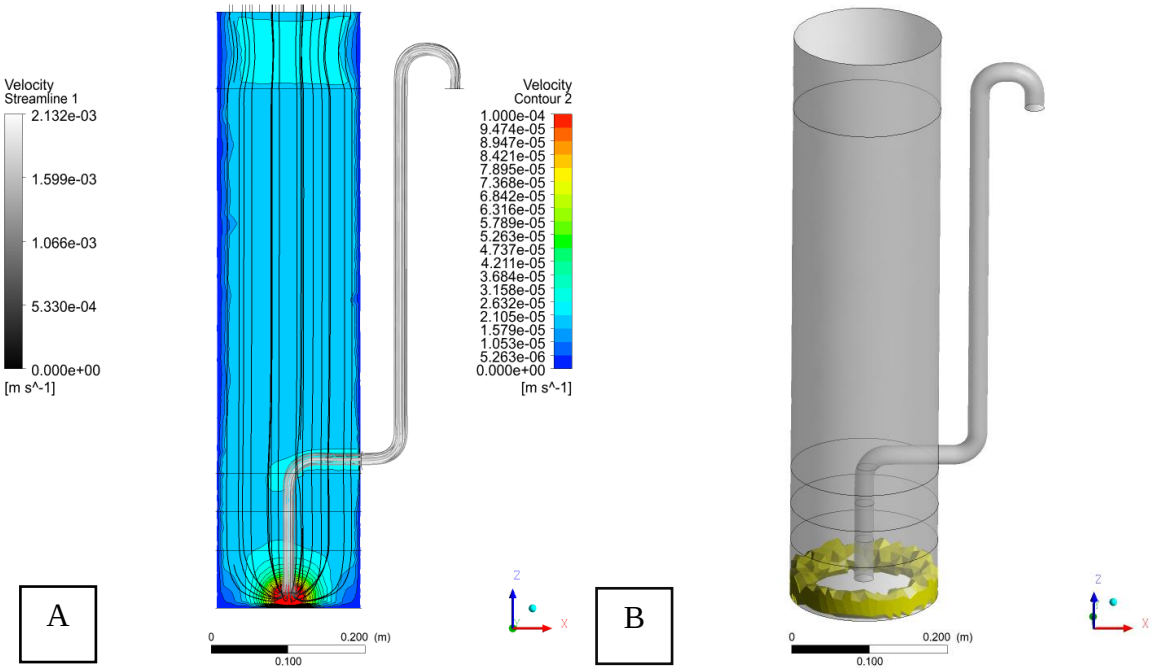

785 Figure S2 – Dead zone in C-HSSF1 (A - Current lines and velocity contour plane; B -

786 Dead zone volume in yellow).

787

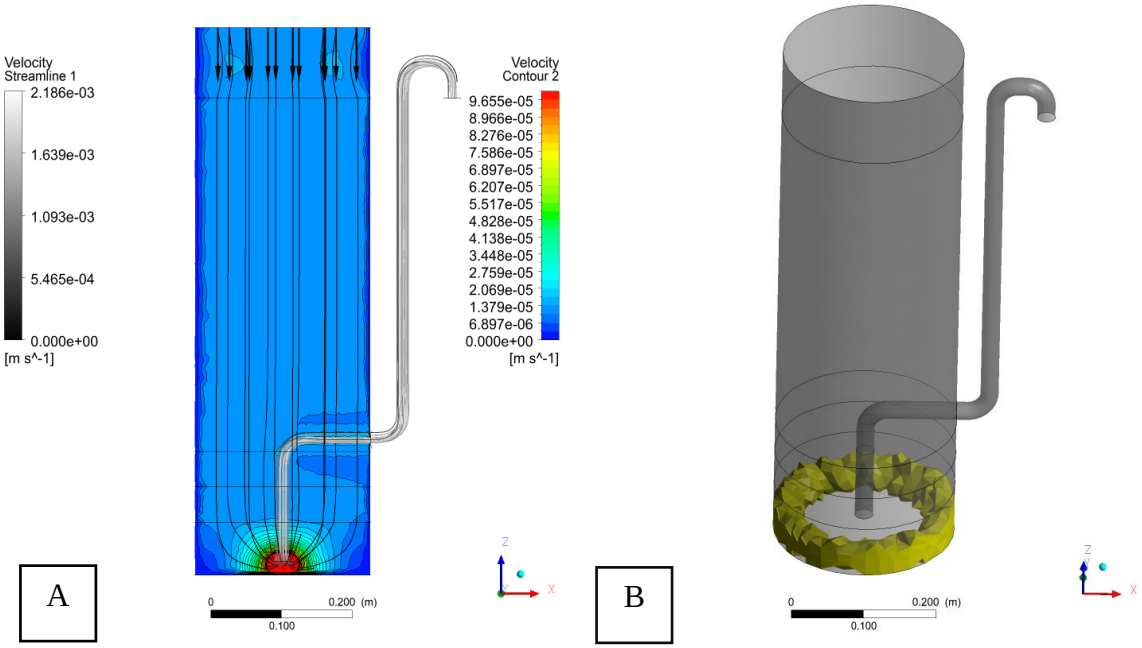

788 Figure S3 – Dead zone in C-HSSF2 (A - Current lines and velocity contour plane; B -

789 Dead zone volume in yellow).

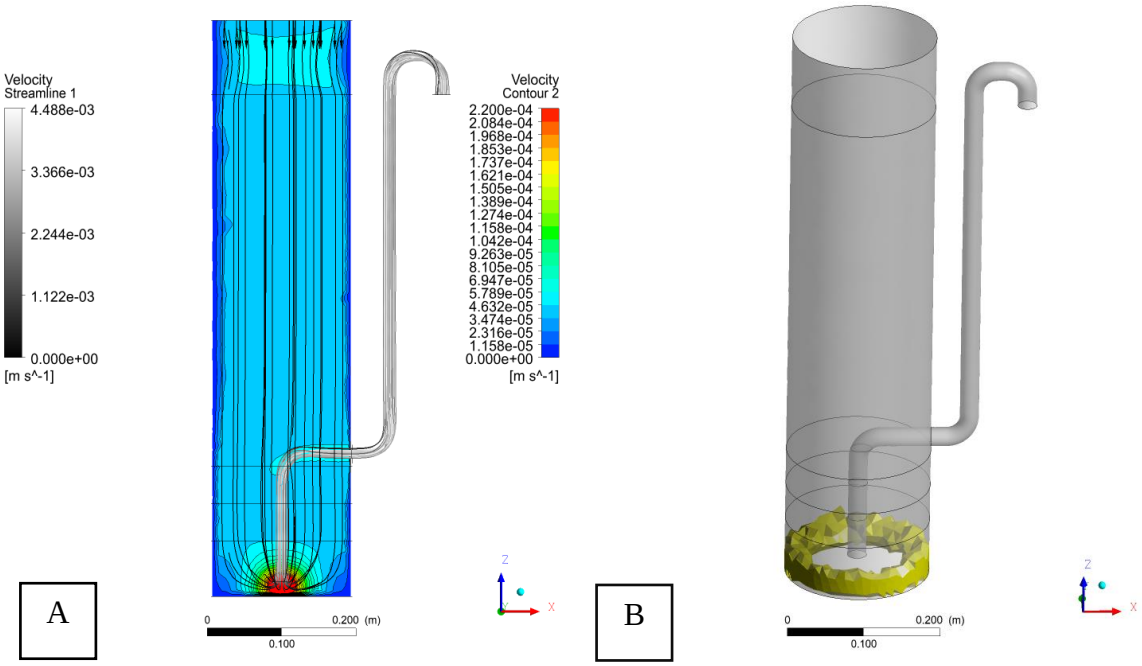

790 Figure S4 – Dead zone in I-HSSF1 (A - Current lines and velocity contour plane; B -

791 Dead zone volume in yellow).

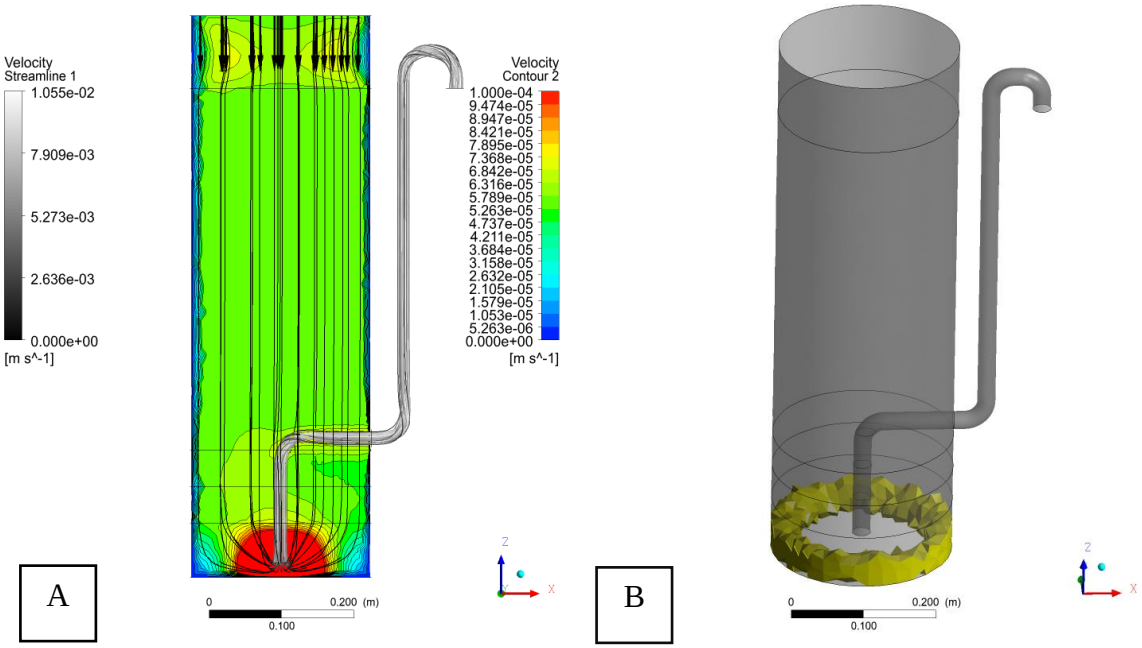

792 Figure S5 – Dead zone on I-HSSF2 (A - Current lines and velocity contour plane; B -
793 Dead zone volume in yellow).

794

795 **References**

796 ABNT NBR 6458. Grãos de pedregulho retidos na peneira de abertura 4,8 mm —
797 Determinação da massa específica, da massa específica aparente e da absorção de água.
798 [Gravel grains retained in the 4.8 mm opening sieve - Determination of specific gravity,
799 apparent specific gravity and water absorption]. Brazil. Rio de Janeiro, 2016.
800 Associação Brasileira de Normas Técnicas - ABNT.

801 ABNT NBR 6502. Rochas e solos. [Rocks and soils]. Brazil. Rio de Janeiro, 1995.
802 Associação Brasileira de Normas Técnicas - ABNT.

803 ABNT NBR 11799. Material filtrante — Areia, antracito e pedregulho —Especificação.
804 [Filter material - Sand, anthracite and gravel - Specification]. Brazil. Rio de Janeiro,
805 2016. Associação Brasileira de Normas Técnicas - ABNT.

ABNT NBR 13292. Solo – Determinação do coeficiente de permeabilidade de solos granulares à carga constante. [Determination of the permeability coefficient of granular soils at constant load]. Brazil. Rio de Janeiro, 1995. Associação Brasileira de Normas Técnicas - ABNT.

ABNT NM 45. Agregados – Determinação da massa unitária e do volume de vazios. [Aggregates - Determination of unit mass and void volume]. Brazil. Rio de Janeiro, 2006. Associação Brasileira de Normas Técnicas - ABNT. Norma Mercosul – NM.

ABNT NM 248. Agregados – Determinação da composição granulométrica. [Aggregates - Determination of particle size composition]. Brazil. Rio de Janeiro, 2001. Associação Brasileira de Normas Técnicas - ABNT. Norma Mercosul – NM.